Northumbria Research Link

Zinc cobalt sulfide nanoparticles as high performance electrode material for asymmetric supercapacitor

Hao Li[1], Zhijie Li[1*], Mengxuan Sun[1], Zhonglin Wu[1], Wenzhong Shen[2], Yong Qing Fu[3**]

[1]School of Physics, University of Electronic Science and Technology of China, Chengdu, 610054, P. R. China

[2]State Key Laboratory of Coal Conversion, Institute of Coal Chemistry, Chinese Academy of Science, Taiyuan, 030001, P. R. China

[3]Faculty of Engineering and Environment, Northumbria University, Newcastle Upon Tyne, NE1 8ST, UK

Zhijie Li (**Corresponding Author**): ORCID: 0000-0001-9870-9939;

*E-mail: zhijieli@uestc.edu.cn; TEL: +86 02883202160

Yong Qing Fu (**Corresponding Author**): ORCID: 0000-0001-9797-4036;

*E-mail: Richard.fu@northumbria.ac.uk; TEL: +44 (0)191 2274662

Abstract

Zinc cobalt sulfide (ZCS) is a promising and high performance electrode material for pseudocapacitors due to its good electrical conductivity, abundant active sites and rich valence states. In this work, zinc cobalt oxide (ZCO) nanoparticles are firstly synthesized *via* a hydrothermal method assisted by hexadecyltrimethyl ammonium bromide (CTAB), and then transformed into zinc cobalt sulfide nanoparticles (ZCS NPs) using a facile sulfuration process. The average diameter of ZCS NPs is estimated to be about 15 nm, which is beneficial for Faradaic redox reactions in energy storage process due to their numerous active surfaces. The ZCS NPs are then coated onto a nickel foam to form the working electrode of supercapacitors. Because the ZCS electrode has lower series and charge transfer resistance, and also higher ion diffusion rate than that of the ZCO electrode, it achieves a large specific capacitance of 1269.1 F g^{-1} at 0.5 A g^{-1} in 2 M KOH electrolyte, which is four times more than that of the ZCO electrode (e.g., 295.8 F g^{-1} at 0.5 A g^{-1}). In addition, an asymmetric supercapacitor using the ZCS NPs as the positive electrode and activated carbon as the negative electrode is assembled, which delivers a high energy density of 45.4 Wh kg^{-1} at a power density of 805.0 W kg^{-1}, with an excellent cycling stability (91.6 % retention of the initial capacitance over 5000 cycles).

Key word: Zinc cobalt sulfide, Hydrothermal method, Nanoparticles, Electrochemical performance, Supercapacitor.

1 Introduction

Because of their fast charge/discharge speeds, high power density, excellent cycling stability and friendly environmental features, supercapacitors (SCs) have received great attention recently [1-3]. According to charge storage mechanisms, the SCs are mainly separated into two categories: electrical double layer capacitors (EDLCs) and pseudocapacitors (PCs). The charge storage mechanism of the EDLCs (which mainly utilize carbon or its derivatives as electrode materials) is based on charge absorption/desorption at electrode/electrolyte interfaces, and the EDLCs generally show remarkable cyclic stability in long-term charge/discharge processes [4]. Whereas the PCs usually provide high capacitances due to the faradic redox reactions of the electrode materials. A variety of materials, such as metal oxides/hydroxides, metal sulfides and conducting polymers have been investigated as electrode materials for the PCs. Among them, ternary metal oxides, for examples, $NiCo_2O_4$, $CuCo_2O_4$, $MnCo_2O_4$ and $ZnCo_2O_4$, attract widespread attention due to their low cost and high theoretical capacitance [5-10]. However, experimentally obtained specific capacitances of these ternary metal oxides are generally much lower than their theoretical values, and due to their low activation energy and low electrical conductivity, these ternary metal oxides often have problems of poor rate capability and cyclic stability [11, 12].

Due to their high electrical conductivity, abundant electrochemical active sites and mechanical/thermal stability, ternary metal sulfides were reported to achieve superior capacitance values and thus have been regarded as one of the promising electrode materials for PCs [13]. In addition, because of the lower electronegativity of sulfur

compared to that of oxygen, the replacement of oxygen with sulfur can bring flexibility in structural design, reduce chances of structural damage, and thus achieve a better stability in long-term charge/discharge processes [14].

So far, studies of ternary metal sulfides are mainly focused on $NiCo_2S_4$, $CuCo_2S_4$, $MnCo_2S_4$ and $FeCo_2S_4$ [15-20]. Among these ternary metal sulfides, the zinc cobalt sulfide (ZCS) electrode materials exhibit good electrochemical performance, due to their rich redox properties through synergistic effects from different metal ions and abundant valence states. For examples, Tao et al synthesized ZCS nanosheet arrays directly on nickel foam, and obtained a very large specific capacitance of 2354.3 F g^{-1} at 0.5 A g^{-1} [21]. Li et al prepared ZCS flowerlike nanoclusters directly on the nickel foam using a hydrothermal approach, and achieved a specific capacitance of 2176.7 F g^{-1} at 1.0 A g^{-1} [22]. These reported ZCS electrode materials showed superior capacitance values. However, they are grown directly on the nickel foam. When these ZCS materials were prepared and then coated onto the commonly used nickel foam, they often showed much less specific capacitance. For examples, the specific capacitance of ZCS nanosheets coated on the nickel foam was 355.3 F g^{-1}, which is much lower than 2354.6 F g^{-1} of the ZCS nanosheet array directly grown on the nickel foam [21]. ZCS nano-artichokes were synthesized by Yang et al using a facile oil phase approach and then coated onto the nickel foam, and achieved a specific capacitance of 486.2 F g^{-1} at 2.0 A g^{-1} [23]. Vignesh et al prepared Ni-Co-Zn-S microspheres through a facile hydrothermal method and then coated them onto the nickel foam to obtain the electrodes, which exhibited a maximum specific capacitance of 825.0 F g^{-1} at 1 A g^{-1}

[24]. Clearly, when these ZCS electrode materials are prepared and then coated onto the current collector to form the electrodes, their specific capacitance values need to be significantly improved. In addition, the quantity of electrode materials directly grown on the nickel foam is usually very limited, which is unsuitable for large-scale industrial applications [25]. So far, there are some studies to prepare ZCS electrode materials, including nanosheets, nanoflowers, microspheres and nano-artichokes [21-24], however, the ZCS nanoparticles have not been reported in literature as the electrode materials for SCs.

In this study, zinc cobalt sulfide nanoparticles (ZCS NPs) were prepared and coated onto nickel foam to form a high performance working electrode for supercapacitor. The zinc cobalt oxide (ZCO) precursor with abundant mesopores and large specific surface area were synthesized using CTAB assisted facile hydrothermal method, and then transformed into ZCS NPs *via* a sulfuration process. The small diameter (about 15 nm) of the ZCS NPs provide more active sites on their surfaces, which are beneficial for Faradaic redox reactions in energy storage processes. Due to the reduced series and charge transfer resistances and increased ion diffusion rate, the obtained electrode based on ZCS NPs showed a much larger specific capacitance than that of the ZCO electrode. Moreover, an asymmetrical supercapacitor (ASC) was assembled using ZCS NPs and active carbon (AC) as the positive and negative electrodes, respectively, and showed both higher energy and power densities and excellent cyclic stability.

2 Experimental details

2.1 Preparation of ZCO and ZCS NPs

All the chemical regents were of analytical purity grade, and used without any further purification. The ZCO were prepared using a facile hydrothermal process. In a typical experiment, 0.446 g $Zn(NO_3)_2 \cdot 6H_2O$ and 0.873 g $Co(NO_3)_2 \cdot 6H_2O$ were dispersed in 75 mL mixed solution (45 mL deionized water and 30 mL ethanol) and magnetically stirred for 10 min. Then, 0.541 g urea and 0.547 g hexadecyltrimethyl ammonium bromide (CTAB) were added into the above solution and further stirred for 30 min. The above mixture was transferred into a 100 mL Teflon-lined stainless-steel autoclave and kept in an oven at 160°C for 12 h for the hydrothermal reaction. After cooled down to the room temperature, the ZCO was obtained by washing the precipitates with the mixed solution of deionized water and ethanol for three times and dried at 80°C for 12 h.

The ZCO were transformed into ZCS NPs *via* a sulfuration process. To achieve this sulfuration process, 0.10 g ZCO and 1.50 g $Na_2S \cdot 9H_2O$ were dissolved in 75 mL deionized water and stirred for 10 min. Then the solution was transferred into a 100 mL Telflon-lined autoclave and kept in an oven at 120°C for 6 h for the hydrothermal reaction. The ZCS NPs were obtained by washing the product with deionized water for three times and dried in a vacuum oven at 50°C for 12 h.

In addition, pure cobalt sulfide and pure zinc sulfide were also prepared through the above hydrothermal process by using 1.309 g $Co(NO_3)_2 \cdot 6H_2O$ and 1.338 g $Zn(NO_3)_2 \cdot 6H_2O$, respectively.

2.2 Materials characterization

Crystalline structures and average crystal sizes of the obtained products were characterized using X-ray diffraction (XRD, Cu Kα, 40 kV, 60 mA, Rigaku D/max-

2400). Their microstructure and morphology were characterized using a transmission electron microscope (TEM, JEM-2200FS) and a scanning electron microscope (SEM, Inspect F50). Chemical states of elements were analyzed using X-ray photoelectron spectroscopy (XPS, KratosAxis-Ultra DLD) with a monochromatic Al Kα radiation. The specific surface areas and pore sizes of the products were measured using a N_2 adsorption-desorption method (Quantachrome, IQ3), and were determined using the Brunauer-Emmett-Teller (BET) and density functional theory (DFT).

2.3 Electrochemical characterization

Electrochemical characterizations including cyclic voltammetry (CV), galvanostatic charge-discharge (GCD) and electrochemical impedance spectroscopy (EIS) of the ZCO and ZCS electrodes were tested using an electrochemical workstation (CHI 660E, Shanghai Chenhua Instrument Co., China) with a three-electrode configuration. The CV tests were performed with the scan rates ranging from 5 to 50 mV s^{-1}. The GCD curves were recorded with the current densities ranging from 0.5 to 10.0 A g^{-1}. The EIS was conducted at open circuit voltage with an amplitude of 5 mV over the frequency range of 10^{-2} to 10^5 Hz. The slurry (80 wt% as-prepared electrode material, 10 wt% polytetrafluoroethylene (PTFE) and 10 wt% carbon black in ethanol) was coated onto a piece of nickel foam (1 × 1 cm^{-2}), and dried at 50°C in a vacuum oven for 12 h. The above nickel foam with active materials was used as the working electrode after they were pressed at 10 MPa for 1 min, and the platinum plate, Hg/HgO and 2 M KOH aqueous solution were used as the counter electrode, reference electrode and electrolyte, respectively.

An asymmetric supercapacitor (ASC) was further fabricated and then tested in a two-electrode configuration. It was assembled with the as-prepared electrode material as the positive electrode, active carbon (AC) as the negative electrode, 2 M KOH aqueous solution as the electrolyte and a piece of cellulose paper as the separator. According to the charge balance theory of the positive and negative electrodes, the mass loading ratio of as-prepared electrode material and AC is determined using the following equation [26]:

$$\frac{m_+}{m_-} = \frac{C_- \times \Delta V_-}{C_+ \times \Delta V_+} \tag{1}$$

where m_+ and m_- are the mass loadings (mg) of the positive and negative electrode materials. C_+, C_- and ΔV_+, ΔV_- are the specific capacitances (F g^{-1}) and potential windows (V) of the positive and negative electrodes, respectively.

3 Results and discussion

3.1 Structural and morphological studies of ZCO and ZCS NPs

Fig. 1 shows the XRD results of the as-prepared ZCO and ZCS NPs, which reveal their phase structures and crystallinity. For ZCO, the main diffraction peaks located at 31.2º, 36.8º, 44.7º, 55.6º, 59.3º and 65.1º are indexed to (220), (311), (400), (422), (511) and (440) planes of $ZnCo_2O_4$ crystals (JCPDS card No. 23-1390). Other minor peaks are corresponding to the zinc carbonate hydroxide hydrate ($Zn_4CO_3(OH)_6 \cdot H_2O$, JCPDS card No. 11-0287). Therefore, the zinc cobalt precursor before the sulfuration process is mainly $ZnCo_2O_4$ with small amounts of $Zn_4CO_3(OH)_6 \cdot H_2O$. All the diffraction peaks of ZCS NPs at 28.6º, 33.2º, 47.6º, 56.5º, 69.7º and 77.0º are corresponding to (111), (200), (220), (311), (400) and (331) planes of $Zn_{0.76}Co_{0.24}S$ (JCPDS card No. 47-1656),

indicating that the $ZnCo_2O_4$ precursor are transformed into $Zn_{0.76}Co_{0.24}S$ phase after the sulfuration process. The average crystal sizes (L) of both the ZCO and ZCS NPs can be estimated using the Scherrer formula [27]:

$$L = \frac{K\lambda}{\beta\cos\theta} \qquad (2)$$

where K is a constant (0.89), λ is the X-ray wavelength (0.15406 nm), β is the line width of peak at half maximum height and θ is the diffraction angle. Based on the Scherrer formula, the estimated crystal sizes of the ZCO and ZCS NPs are 48.0 and 16.3 nm, respectively, indicating that the microstructures have been changed apparently after the sulfuration process. The smaller crystal size of the ZCS NPs means that there are abundant active sites on the surfaces of nanoparticles, which is in favor of redox reactions in the energy storage process.

Figs. 2a and 2b display the SEM images of both the ZCO and ZCS NPs, which are composed of numerous nanoparticles. The structures of the ZCS NPs were further investigated using the TEM analysis. As is shown in Figs. 2c and 2d, the average diameter of the ZCS NPs is about ~15 nm, which is in a well agreement with the result obtained from the XRD analysis. The lattice fringes of the HRTEM image shown in Fig. 2e reveal that the lattice spacing is 0.311 nm, which is corresponding to the (111) plane of ZCS NPs. The selected area electron diffraction (SAED) pattern with well defined diffraction rings shown in Fig. 2f proves the polycrystalline nature of these ZCS NPs. These diffraction rings can be assigned to (111), (200), (220) and (311) planes of $Zn_{0.76}Co_{0.24}S$, which can support the XRD results.

The element concentrations of the ZCO and ZCS NPs were obtained using the EDX

analysis. As shown in Fig. 2g, three elements of Zn, Co and O (with their atomic percentages of 10.15%, 14.81% and 75.04%, respectively) are existed in zinc cobalt precursor. Because of the existence of a small amount of $Zn_4CO_3(OH)_6 \cdot H_2O$, the atomic percentages of Zn and Co elements in the sample are different from the ratio in $ZnCo_2O_4$. Fig. 2h shows that the ZCS NPs are composed of Zn, Co and S elements, and their atomic percentages are 13.38%, 25.91% and 60.71% respectively. However, because the $ZnCo_2O_4$ has been transformed into $Zn_{0.76}Co_{0.24}$ and amorphous cobalt sulfides during the sulfuration process, the obtained atomic percentages are different from that of $Zn_{0.76}Co_{0.24}S$ [28]. Therefore, the ZCS NPs are composed of $Zn_{0.76}Co_{0.24}S$ and amorphous cobalt sulfide.

Chemical composition and chemical states of the ZCO and ZCS NPs were characterized using XPS. XPS survey spectrum of ZCO shown in Fig. 3a proves the presence of Zn, Co and O elements. The two major peaks at 1044.5 eV and 1021.5 eV in the high-resolution XPS spectrum of Zn 2p (see Fig. 3b) can be assigned to Zn $2p_{1/2}$ and Zn $2p_{3/2}$, respectively, confirming the Zn^{2+} oxidation state in $ZnCo_2O_4$ molecule. As shown in Fig. 3c, high-resolution spectrum of Co 2p has two peaks at 796.9 eV and 780.8 eV with two satellite peaks, which are corresponding to Co $2p_{1/2}$ and Co $2p_{3/2}$ of Co^{3+}, respectively [29]. The high-resolution spectrum of O 1s (Fig. 3d) can be deconvoluted into two type oxygen species. The peak at 531.3 eV can be assigned to the lattice oxygen atoms in $ZnCo_2O_4$, whereas the peak at 529.5 eV is the characteristic peak of –OH species [30, 31].
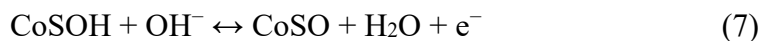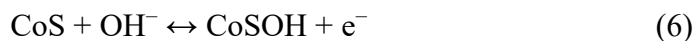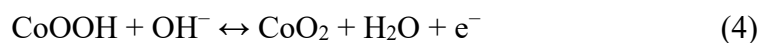
Fig. 4a shows the survey spectrum of ZCS NPs, which confirms the presence of Zn,

Co, S, O and C elements. The existence of elements of O and C are mainly due to the surface adsorption from the air [21, 32]. The high-resolution spectrum of Zn 2p shown in Fig. 4b demonstrates two strong peaks at 1044.5 eV and 1021.4 eV, which are assigned to Zn $2p_{1/2}$ and Zn $2p_{3/2}$. These peak positions are associated to the Zn^{2+} ion in the ZCS NPs [14]. The spectrum of Co 2p in Fig. 4c can be deconvoluted into two satellite peaks and four spin-orbit doublets, indicating the co-existence of Co^{2+} and Co^{3+} ions in the ZCS NPs [33]. The peaks at the binding energies of 793.4 eV and 778.3 eV are assigned to Co^{3+}, while the peaks at 798.0 eV and 781.9 eV can be assigned to Co^{2+} [34]. The peaks at 802.7 eV and 785.7 eV are the satellite peaks of Co^{3+} and Co^{2+} [35, 36]. For the high resolution spectrum of S 2p shown in Fig. 4d, the peak at 169.7 eV is assigned to the shake-up satellite peak of S 2p, indicating the existence of S^{2-} ion in the ZCS NPs, and the peaks at 162.5 eV and 161.4 eV are belonged to S $2p_{3/2}$ and S $2p_{1/2}$, respectively [14, 37]. From the XPS analysis, the chemical states of the ZCS NPs contain Zn^{2+}, Co^{2+}, Co^{3+} and S^{2-}, which are in good agreements with the results obtained from the XRD characterization of the $Zn_{0.76}Co_{0.24}S$.

The BET surface area and pore size distribution of the ZCO and ZCS NPs were measured according to the N_2 adsorption-desorption isotherms and the results are shown in Fig. S1. The BET surface areas of both the ZCO and ZCS NPs are 35.4 m^2 g^{-1} and 11.4 m^2 g^{-1}, respectively. As shown in Fig. S1a, a mesoporous structure was formed in ZCO, which is mainly due to the accumulation of nanoparticles. The pore size distribution is centered at ~21.4 nm. However, no clear porous structure was found in the ZCS NPs from the N_2 adsorption-desorption isotherms as shown in Fig. S1b.

3.2 Electrochemical properties of electrodes based on ZCO and ZCS NPs

The CV curves of both the ZCO and ZCS electrodes at different scan rates from 5 to 50 mV s^{-1} are presented in Figs. 5a and 5b, respectively, in a potential window of 0 to 0.6 V (vs. Hg/HgO). It can be seen that all the CV curves exhibit obvious redox peaks, indicating the dominant Faradaic reaction behaviors for both the ZCO and ZCS electrodes during the energy charge/discharge process [38]. The Faradaic reaction behaviors of the electrodes can be described using equations (3) and (4) for the ZCO electrode, and equations (5)~(7) for the ZCS electrode [39-41]:

$$ZnCo_2O_4 + OH^- + H_2O \leftrightarrow ZnOOH + 2CoOOH + e^- \tag{3}$$

$$CoOOH + OH^- \leftrightarrow CoO_2 + H_2O + e^- \tag{4}$$

$$Zn_{0.76}Co_{0.24}S + OH^- \leftrightarrow 0.76ZnSOH + 0.24CoSOH + e^- \tag{5}$$

$$CoS + OH^- \leftrightarrow CoSOH + e^- \tag{6}$$

$$CoSOH + OH^- \leftrightarrow CoSO + H_2O + e^- \tag{7}$$

The shape of CV curves is only changed slightly as the scan rate is increased from 5 to 50 mV s^{-1}, which demonstrates the good rate capabilities for these two electrode materials [42]. Due to the rapid electronic/ionic transports, the positions of cathodic and anodic peaks are shifted to negative and positive potentials when the scan rate is increased [43]. Based on the CV data, the good linearity between square root of scan rate and peak current density of anodic/cathodic reaction from 5 to 50 mV s^{-1} was obtained and the results are shown in Figs. 5c and 5d, indicating that the electrochemical processes of both ZCO and ZCS electrode are controlled by the diffusion of OH$^-$ from electrolyte to electrode surface [44]. Figs. 5e and 5f show the

GCD curves of both the ZCO and ZCS electrodes at different current densities. The formation of plateaus in charge/discharge curves of ZCO and ZCS electrodes also suggests the typical characteristics of Faradaic reactions, which are consistent with the results obtained from the CV curves.

Figs. 6a and 6b exhibit the CV and GCD curves of ZCO and ZCS electrodes at a scan rate of 10 mV s^{-1} and a current density of 0.5 A g^{-1}, respectively. The CV's integrated area and GCD's discharge time for the ZCS electrode are found to be much larger than that of the ZCO electrode, indicating that the ZCS electrode can generate much higher specific capacitance values than the ZCO electrode. The specific capacitance values (C_s, F g^{-1}) of both the ZCO and ZCS electrodes can be calculated by the formula (8) based on the GCD curves [45, 46]:

$$C_s = \frac{I \times \varDelta t}{m \times \varDelta V} \tag{8}$$

where $\varDelta t$ (s) is the discharge time, I (mA) is the discharge current, $\varDelta V$ (V) is the potential window and m (mg) is the mass of the electrode material. Using the GCD measurement data, the specific capacitance values of the ZCO and ZCS electrodes were calculated to be 295.8 and 1269.1 F g^{-1}, respectively, at a current density of 0.5 A g^{-1}. It clearly demonstrates that the specific capacitance of ZCS electrode have been significantly increased after the sulfuration process.

Therefore, although the ZCO has larger specific surface areas and more mesoporous structures than that of the ZCS NPs, the ZCS electrode has remarkably higher specific capacitance values than the ZCO. The abundant active sites generated on the surfaces of ZCS NPs due to the smaller crystal size is one of the reasons. The large capacitance

13

value of the ZCS electrode should also be attributed to the lower electronic resistance of the ZCS electrode compared to that of the ZCO electrode. To further investigate the electrochemical characteristics of electrode materials, EIS measurement was carried out, and the obtained Nyquist plots of the ZCO and ZCS electrodes in the frequency range of 10^{-2} to 10^5 Hz are shown in Fig. 6c. The equivalent circuit model which is consisted of series resistance (R_s), charge-transfer resistance (R_{ct}), constant phase element (CPE) and Warburg impedance (W) is shown in the insert of Fig. 6c. All the EIS spectra are consisted of a straight line in the low frequency region and a semicircle in the high frequency region, demonstrating the typical capacitive characteristics for both the ZCO and ZCS electrodes. It is well reported that the slope of the straight line in the lower frequency region represents the value of W, which is linked with the ion diffusion in the electrolyte to the electrode interface. The diameter of the semicircle in the high frequency region is associated with the R_{ct}, which is related to the electron transfer kinetics of the redox reaction at the electrode/electrolyte interface [47, 48]. In addition, the intercept at the real axis in the high frequency region represents the R_s, which is the combination of intrinsic resistance of electrode materials/electrolyte, and contact resistance between electrode materials and current collector [49]. On the basis of an equivalent circuit and theoretically fitted results, the obtained R_s and R_{ct} values of the ZCS electrode are about 1.06 Ω and 0.37 Ω, respectively, which are smaller than those of the ZCO electrode (e.g., Rs: 1.43 Ω, Rct: 2.64 Ω). The result shows that the ZCS electrode has low series resistances and fast charge-transfer rate, which is due to the abundant electrochemical active sites of the binary metal sulfides. Moreover, the slope

14

of the straight line of the ZCS electrode is larger than that of the ZCO electrode in the lower frequency region, indicating that ion diffusion rate of the ZCS electrode is higher than that of the ZCO electrode [50, 51]. Therefore, the ZCS electrode has a much lower electronic resistance than the ZCO electrode, which is beneficial to the increase of specific capacitance value.

In addition, the specific capacitance values of both the ZCO and ZCS electrodes were obtained at different current densities, and the results are shown in Fig. 6d. The obtained data are 295.8, 287.1, 266.5, 244.8, 229.2, 217.1 and 206.2 F g^{-1} for the ZCO electrode and 1269.1, 1140.7, 1008.9, 891.3, 819.7, 760.3 and 711.1 F g^{-1} for the ZCS electrode at different current densities of 0.5, 1, 2, 4, 6, 8 and 10 A g^{-1}. Clearly, the specific capacitances values are decreased with the increase of current densities. The reason is that the electrolyte ions are sufficiently diffused onto the active sites of electrode material at lower current densities, thus leading to sufficient redox reactions generated on the surface of electrode material. However, at higher current densities, the electrolyte ions cannot be sufficiently diffused into the active sites of electrode material, thus leading to insufficient redox reactions [52]. Therefore, due to the smaller specific surface areas of ZCS than that of ZCO, the efficiency of electrolyte ions diffused into the ZCS NPs will be lower than that of the ZCO NPs at higher current densities. This has resulted that the rate capacity of the ZCS electrode is smaller than that of the ZCO electrode. Fig. 6e shows the specific capacitance of the ZCS NPs electrode after 5000 GCD cycles operated at a high current density of 10 A g^{-1}. It can be seen that the retention of the specific capacitance is 93.5% after 5000 cycles, indicating it has

excellent cycling performance.

For comparisons, the electrochemical performances of cobalt sulfide electrode and zinc sulfide electrode has also been investigated, and their CV curves, GCD curves, specific capacitances with different current densities and Nyquist plots are shown in Figs. S2 and S3. As shown in Fig. S2a and Fig. S3a, all the CV curves exhibit obvious redox peaks, indicating that the key energy storage mechanism for these two electrodes are Faradaic redox reaction. Based on the GCD curves measured at different current densities shown in Figs. S2b and S3b, The calculated specific capacitances for both cobalt sulfide and zinc sulfide electrodes are 591.7 and 130.8 F g^{-1} at a current density of 0.5 A g^{-1} (see Fig. S2c and Fig. S 3c), which are much lower than that of the ZCS NPs electrode (1269.1 F g^{-1}).

3.3 Electrochemical performance of ZCS NPs//AC asymmetric supercapacitor

Fig. 7a shows the electrochemical properties of asymmetric supercapacitor (ASC, two-electrode system), which was assembled to investigate the practical application of the ZCS electrode. The CV curves of both the AC and ZCS electrodes tested at a scan rate of 10 mV s^{-1} are displayed in Fig. 7b. It can be seen that the potential windows of AC and ZCS NPs are -1~0 V and 0~0.6 V, respectively, indicating that the ZCS NPs//AC ASC can be operated at a potential window of 0~1.6 V. Fig. 7c shows the CV curves of the ZCS NPs//AC ASC in different potential windows from 0.8~1.6 V. At the highest voltage of 1.6 V, a slight polarization phenomenon can be observed. Therefore, in this study, the suitable operation potential window is ranged from 0~1.6 V, which was used further to investigate the electrochemical performance of the ZCS NPs//AC

ASC.

The GCD curves as shown in Fig. 7d reveal that the ASC can work stably at the highest voltage of 1.6 V, which is in a good agreement with CV curves. Fig. 7e shows the CV curves of the ZCS NPs//AC ASC tested at different scan rates. It can be seen that all the CV curves have obvious redox peaks, indicating that the dominant mechanism of energy storage of the ZCS NPs//AC ASC is redox reaction generated from the Faradaic process. Fig. 7f shows the GCD curves of the ZCS NPs//AC ASC obtained at different current densities, and the specific capacitance (C_d) can be obtained using the following formula (9):

$$C_d = \frac{I \times \Delta t}{M \times \Delta V} \tag{9}$$

where I, Δt and ΔV are the current (mA), discharge time (s) and potential window (V) of the ASC, and M (mg) is the total mass of both the positive and negative electrodes.

The values of the calculated specific capacitances of ZCS NPs//AC ASC are 127.7, 119.7, 113.3, 109.5, 106.8 and 104.7 F g^{-1} measured at 1, 2, 4, 6, 8 and 10 A g^{-1}, respectively, which have also been shown in Fig. 8a. Results demonstrate that ~82.0 % retention of the initial capacitance can be achieved when the current density was increased from 1 to 10 A g^{-1}, indicating the good rate capacity of the ZCS NPs//AC ASC. The energy density (E, Wh kg^{-1}) and power density (P, W kg^{-1}) of the ASC can be calculated using formula (10) and (11) [53-55]:

$$E = \frac{C_d \times \Delta V^2}{2 \times 3.6} \tag{10}$$

$$P = \frac{E \times 3600}{\Delta t} \tag{11}$$

where ΔV and Δt are the potential window (V) and discharge time (s) of the ASC,

respectively. Based on the specific capacitance values obtained at different current densities, the Ragone plots of the ZCS NPs//AC ASC can be obtained and the results are shown in Fig. 8b. Notably, the ASC displays a high energy density of 45.4 Wh kg^{-1} at a power density of 805.0 W kg^{-1}. Even at a much higher power density of 8533.3 W kg^{-1}, the device still show an energy density of 37.2 Wh kg^{-1}. These results are much better than those of ASCs reported previously in literature, for examples, Zn-Co-S//AC (31.9 Wh kg^{-1} at 850.0 W kg^{-1}) [21], $NiCo_2S_4@VS_2$//AC (31.2 Wh kg^{-1} at 775.0 W kg^{-1}) [56], $PCs/NiCo_2S_4$//AC (23.3 Wh kg^{-1} at 335.8 W kg^{-1}) [57], Co_9S_8/graphene//rGO (37.0 Wh kg^{-1} at 1800.0 W kg^{-1}) [58] and Ni_3S_4//AC (18.6 Wh kg^{-1} at 1500.2 W kg^{-1}) [59]. Furthermore, the ASC maintains a high capacitance retention ratio of about 91.6 % after 5000 charge/discharge cycles operated at 10 A g^{-1} as shown in Fig. 8c, indicating the superior cyclic stability of the ZCS NPs//AC ASC. Finally, two ZCS NPs//AC ASC assembled in series can easily light up a red light-emitting diode (LED) as demonstrated in Fig. 8d.

4 Conclusions

In summary, ZCS NPs have been successfully synthesized using a two-step hydrothermal and sulfuration method. Due to the lower series and charge-transfer resistance, and abundant active sites, the prepared ZCS electrode exhibits a high specific capacitance of 1269.1 F g^{-1} at 0.5 A g^{-1}, which is more than four times larger than that of the ZCO electrode (295.8 F g^{-1} at 0.5 A g^{-1}). A ZCS NPs//AC ASC was assembled and achieved the maximum energy density of 45.4 Wh kg^{-1} at the power density of 805.0 W kg^{-1} and the capacitance retention of 91.6 % after 5000

charge/discharge cycles. These results suggest that the ZCS NPs is a promising electrode material for high-performance supercapacitor application.

Acknowledgments

References

[1] H. L. Zhu, Y. Q. Zheng, Mesoporous Co_3O_4 anchored on the graphitic carbon nitride for enhanced performance supercapacitor, Electrochim. Acta, 265 (2018) 372-378.

[2] X. Li, M. Zhang, L. Wu, Q. Fu, H. Gao, Annealing temperature dependent $ZnCo_2O_4$ nanosheet arrays supported on Ni foam for high-performance asymmetric supercapacitor, J. Alloy. Compd., 773 (2019) 367-375.

[3] H. Si, L. Sun, Y. Zhang, Y. Zhang, L. Bai, Y. Zhang, Carbon-coated MoO_2 nanoclusters anchored on RGO sheets as high-performance electrodes for symmetric supercapacitors, Dalton T., 48 (2018) 285-295.

[4] X. Li, Y. Qiao, C. Wang, T. Shen, X. Zhang, H. Wang, Y. Li, W. Gao, MOF-derived Co/C nanocomposites encapsulated by $Ni(OH)_2$ ultrathin nanosheets shell for high performance supercapacitors, J. Alloy. Compd., 770 (2019) 803-812.

[5] W. Qiu, H. Xiao, M. Yu, Y. Li, X. Lu, Surface modulation of $NiCo_2O_4$ nanowire arrays with significantly enhanced reactivity for ultrahigh-energy supercapacitors, Chem. Eng. J., 352 (2018) 996-1003.

[6] Y. Wang, D. Yang, J. Lian, T. Wei, Y. Sun, Ordered corn-like $CuCo_2O_4$ nanoforests covering Ni foam for a high-performance all-solid-state supercapacitor, J. Alloy. Compd., 741 (2018) 527-531.

[7] C. Xiao, X. Zhang, D. R. MacFarlane, Dual-$MnCo_2O_4$/Ni electrode with three-level hierarchy for high-performance electrochemical energy storage, Electrochim. Acta, 280 (2018) 55-61.

[8] D. Song, J. Zhu, J. Li, T. Pu, B. Huang, C. Zhao, L. Xie, L. Chen, Free-standing Two-dimensional Mesoporous $ZnCo_2O_4$ Thin Sheets Consisting of 3D Ultrathin Nanoflake Array Frameworks for High Performance Asymmetric Supercapacitor, Electrochim. Acta, 257 (2017) 455-464.

[9] P. Zhao, X. Ye, Y. Zhu, H. Jiang, L. Wang, Z. Yue, Z. Wan, C. Jia, Three-dimensional ordered macroporous $NiFe_2O_4$ coated carbon yarn for knittable fibriform supercapacitor, Electrochim. Acta, 281 (2018) 717-724.

[10] T.-H. Ko, S. Radhakrishnan, M.-K. Seo, M.-S. Khil, H.-Y. Kim, B.-S. Kim, A green and scalable dry synthesis of $NiCo_2O_4$/graphene nanohybrids for high-performance supercapacitor and enzymeless glucose biosensor applications, J. Alloy. Compd., 696 (2017) 193-200.

[11] J. Zhang, H. Guan, Y. Liu, Y. Zhao, B. Zhang, Hierarchical polypyrrole nanotubes@$NiCo_2S_4$

nanosheets core-shell composites with improved electrochemical performance as supercapacitors, Electrochim. Acta, 258 (2017) 182-191.

[12] X. Y. Yu, X. W. Lou, Mixed Metal Sulfides for Electrochemical Energy Storage and Conversion, Adv. Energy Mater., 8 (2018) 1701592.

[13] H. You, L. Zhang, Y. Jiang, T. Shao, M. Li, J. Gong, Bubble-supported engineering of hierarchical $CuCo_2S_4$ hollow spheres for enhanced electrochemical performance, J. Mater. Chem. A, 6 (2018) 5265-5270.

[14] H. Tong, W. Bai, S. Yue, Z. Gao, L. Lu, L. Shen, S. Dong, J. Zhu, J. He, X. Zhang, Zinc cobalt sulfide nanosheets grown on nitrogen-doped graphene/carbon nanotube film as a high-performance electrode for supercapacitors, J. Mater. Chem. A, 4 (2016) 11256-11263.

[15] J. Lin, Y. Yan, X. Zheng, Z. Zhong, Y. Wang, J. Qi, J. Cao, W. Fei, Y. Huang, J. Feng, Designing and constructing core-shell $NiCo_2S_4@Ni_3S_2$ on Ni foam by facile one-step strategy as advanced battery-type electrodes for supercapattery, J. Colloid Interf. Sci., 536 (2019) 456-462.

[16] S. Cheng, T. Shi, C. Chen, Y. Zhong, Y. Huang, X. Tao, J. Li, G. Liao, Z. Tang, Construction of porous $CuCo_2S_4$ nanorod arrays via anion exchange for high-performance asymmetric supercapacitor, Sci. Rep., 7 (2017) 6681.

[17] A. M. Elshahawy, X. Li, H. Zhang, Y. Hu, K. H. Ho, C. Guan, J. Wang, Controllable $MnCo_2S_4$ nanostructures for high performance hybrid supercapacitors, J. Mater. Chem. A, 5 (2017) 7494-7506.

[18] Y. Huang, Y. Zhao, J. Bao, J. Lian, M. Cheng, H. Li, Lawn-like $FeCo_2S_4$ hollow nanoneedle arrays on flexible carbon nanofiber film as binder-free electrodes for high-performance asymmetric pseudocapacitors, J. Alloy. Compd., 772 (2019) 337-347.

[19] A. Pramanik, S. Maiti, T. Dhawa, M. Sreemany, S. Mahanty, High faradaic charge storage in $ZnCo_2S_4$ film on Ni-foam with a hetero-dimensional microstructure for hybrid supercapacitor, Materials Today Energy, 9 (2018) 416-427.

[20] J. Liao, P. Zou, S. Su, A. Nairan, Y. Wang, D. Wu, C.-P. Wong, F. Kang, C. Yang, Hierarchical nickel nanowire@$NiCo_2S_4$ nanowhisker composite arrays with a test-tube-brush-like structure for high-performance supercapacitors, J. Mater. Chem. A, 6 (2018) 15284-15293.

[21] K. Tao, X. Han, Q. Cheng, Y. Yang, Z. Yang, Q. Ma, L. Han, A Zinc Cobalt Sulfide Nanosheet Array Derived from a 2D Bimetallic Metal-Organic Frameworks for High-Performance Supercapacitors, Chem. Eur. J., 24 (2018) 12584-12591.

[22] Y. Li, H. Gao, Z. Sun, Q. Li, Y. Xu, C. Ge, Y. Cao, Tuning morphology and conductivity in two-step synthesis of zinc-cobalt oxide and sulfide hybrid nanoclusters as highly-performed electrodes for hybrid supercapacitors, J. Solid State Electr., 22 (2018) 3197-3207.

[23] J. Yang, Y. Zhang, C. Sun, G. Guo, W. Sun, W. Huang, Q. Yan, X. Dong, Controlled synthesis of zinc cobalt sulfide nanostructures in oil phase and their potential applications in electrochemical energy storage, J. Mater. Chem. A, 3 (2015) 11462-11470.

[24] V. Vignesh, R. Navamathavan, Spherical-Like Ball-by-Ball Architecture of Ni-Co-Zn-S Electrodes for Electrochemical Energy Storage Application in Supercapacitors, J. Electrochem. Soc., 164 (2017) E434-E439.

[25] J. Xie, P. Yang, Y. Wang, T. Qi, Y. Lei, C.M. Li, Puzzles and confusions in supercapacitor and battery: Theory and solutions, J. Power Sources, 401 (2018) 213-223.

[26] Y. Shao, M.F. El-Kady, J. Sun, Y. Li, Q. Zhang, M. Zhu, H. Wang, B. Dunn, R.B. Kaner, Design and Mechanisms of Asymmetric Supercapacitors, Chem. Rev., 118 (2018) 9233-9280.

[27] Z. Li, Z. Lin, N. Wang, J. Wang, W. Liu, K. Sun, Y. Q. Fu, Z. Wang, High precision NH_3 sensing

using network nano-sheet Co_3O_4 arrays based sensor at room temperature, Sens. Actuators B, 235 (2016) 222-231.

[28] Y. Yang, W. Huang, S. Li, L. Ci, P. Si, Surfactant-dependent flower- and grass-like $Zn_{0.76}Co_{0.24}S/Co_3S_4$ for high-performance all-solid-state asymmetric supercapacitors, J. Mater. Chem. A, 6 (2018) 22830-22839.

[29] T. Liu, W. Wang, M. Yi, Q. Chen, C. Xu, D. Cai, H. Zhan, Metal-organic framework derived porous ternary $ZnCo_2O_4$ nanoplate arrays grown on carbon cloth as binder-free electrodes for lithium-ion batteries, Chem. Eng. J., 354 (2018) 454-462.

[30] J. Qi, J. Mao, A. Zhang, L. Jiang, Y. Sui, Y. He, Q. Meng, F. Wei, X. Zhang, Facile synthesis of mesoporous $ZnCo_2O_4$ nanosheet arrays grown on rGO as binder-free electrode for high-performance asymmetric supercapacitor, J. Mater. Sci., 53 (2018) 16074-16085.

[31] L. Shen, H. Lv, S. Chen, P. Kopold, P. A. van Aken, X. Wu, J. Maier, Y. Yu, Peapod-like Li_3VO_4/N-Doped Carbon Nanowires with Pseudocapacitive Properties as Advanced Materials for High-Energy Lithium-Ion Capacitors, Adv. Mater., 29 (2017) 1700142.

[32] X. Li, J. Cao, L. Yang, M. Wei, X. Liu, Q. Liu, Y. Hong, Y. Zhou, J. Yang, One-pot synthesis of ZnS nanowires/Cu_7S_4 nanoparticles/reduced graphene oxide nanocomposites for supercapacitor and photocatalysis applications, Dalton T., 48 (2019) 2442-2454.

[33] Y. Lu, L. Li, D. Chen, G. Shen, Nanowire-assembled $Co_3O_4@NiCo_2O_4$ architectures for high performance all-solid-state asymmetric supercapacitors, J. Mater. Chem. A, 5 (2017) 24981-24988.

[34] Y. Liu, G. Jiang, S. Sun, B. Xu, J. Zhou, Y. Zhang, J. Yao, Growth of $NiCo_2S_4$ nanotubes on carbon nanofibers for high performance flexible supercapacitors, J. Electroanal. Chem., 804 (2017) 212-219.

[35] Y. Zou, C. Cai, C. Xiang, P. Huang, H. Chu, Z. She, F. Xu, L. Sun, H.-B. Kraatz, Simple synthesis of core-shell structure of Co–Co_3O_4@carbon-nanotube-incorporated nitrogen-doped carbon for high-performance supercapacitor, Electrochim. Acta, 261 (2018) 537-547.

[36] H. Chen, M.Q. Wang, Y. Yu, H. Liu, S.Y. Lu, S.J. Bao, M. Xu, Assembling Hollow Cobalt Sulfide Nanocages Array on Graphene-like Manganese Dioxide Nanosheets for Superior Electrochemical Capacitors, ACS Appl. Mater. Inter., 9 (2017) 35040-35047.

[37] L. Shen, J. Wang, G. Xu, H. Li, H. Dou, X. Zhang, $NiCo_2S_4$ Nanosheets Grown on Nitrogen-Doped Carbon Foams as an Advanced Electrode for Supercapacitors, Adv. Energy Mater., 5 (2015) 1400977.

[38] P. Zhang, B. Y. Guan, L. Yu, X. W. Lou, Formation of Double-Shelled Zinc-Cobalt Sulfide Dodecahedral Cages from Bimetallic Zeolitic Imidazolate Frameworks for Hybrid Supercapacitors, Angew. Chem. Int. Ed., 56 (2017) 7141-7145.

[39] Y. Lv, A. Liu, Z. Shi, H. Che, J. Mu, Z. Guo, X. Zhang, Construction of hierarchical zinc cobalt sulfide@nickel sulfide core-shell nanosheet arrays for high-performance asymmetric solid-state supercapacitors, Chem. Eng. J., 349 (2018) 397-407.

[40] H. Chen, J. Wang, X. Han, F. Liao, Y. Zhang, L. Gao, C. Xu, Facile synthesis of mesoporous $ZnCo_2O_4$ hierarchical microspheres and their excellent supercapacitor performance, Ceram. Int., 45 (2019) 8577-8584.

[41] L. Shen, L. Yu, H.B. Wu, X.Y. Yu, X. Zhang, X.W. Lou, Formation of nickel cobalt sulfide ball-in-ball hollow spheres with enhanced electrochemical pseudocapacitive properties, Nat. Commun., 6 (2015) 6694.

[42] M. Sharma, S. Sundriyal, A.K. Panwar, A. Gaur, Facile synthesis and electrochemical performance of Mg-substituted $Ni_{1-x}Mg_xCo_2O_4$ mesoporous nanoflakes for energy storage applications, Electrochim. Acta, 294 (2019) 53-59.

[43] Z. Qu, M. Shi, H. Wu, Y. Liu, J. Jiang, C. Yan, An efficient binder-free electrode with multiple carbonized channels wrapped by $NiCo_2O_4$ nanosheets for high-performance capacitive energy storage, J. Power Sources, 410-411 (2019) 179-187.

[44] L. Saleh Ghadimi, N. Arsalani, A.G. Tabrizi, A. Mohammadi, I. Ahadzadeh, Novel nanocomposite of $MnFe_2O_4$ and nitrogen-doped carbon from polyaniline carbonization as electrode material for symmetric ultra-stable supercapacitor, Electrochim. Acta, 282 (2018) 116-127.

[45] B. Gnana Sundara Raj, H.-Y. Kim, B.-S. Kim, Ultrasound assisted formation of Mn_2SnO_4 nanocube as electrodes for high performance symmetrical hybrid supercapacitors, Electrochim. Acta, 278 (2018) 93-105.

[46] L. D. Chen, Y. Q. Zheng, H. L. Zhu, Manganese oxides derived from Mn(II)-based metal–organic framework as supercapacitor electrode materials, J. Mater. Sci., 53 (2017) 1346-1355.

[47] Q. Zhang, H. Liu, Y. Xu, L. Wang, 3D nanoflower-like zinc hydroxyl carbonates for high performance asymmetric supercapacitors, J. Solid State Chem., 267 (2018) 76-84.

[48] F. Ochai-Ejeh, M.J. Madito, K. Makgopa, M.N. Rantho, O. Olaniyan, N. Manyala, Electrochemical performance of hybrid supercapacitor device based on birnessite-type manganese oxide decorated on uncapped carbon nanotubes and porous activated carbon nanostructures, Electrochim. Acta, 289 (2018) 363-375.

[49] Y. Liu, Z. Zhou, S. Zhang, W. Luo, G. Zhang, Controllable synthesis of CuS hollow microflowers hierarchical structures for asymmetric supercapacitors, Appl. Surf. Sci., 442 (2018) 711-719.

[50] X. X. Li, X. H. Deng, Q. J. Li, S. Huang, K. Xiao, Z. Q. Liu, Y. Tong, Hierarchical double-shelled poly(3,4-ethylenedioxythiophene) and MnO_2 decorated Ni nanotube arrays for durable and enhanced energy storage in supercapacitors, Electrochim. Acta, 264 (2018) 46-52.

[51] B. Huang, W. Wang, T. Pu, J. Li, J. Zhu, C. Zhao, L. Xie, L. Chen, Two-dimensional porous (Co, Ni)-based monometallic hydroxides and bimetallic layered double hydroxides thin sheets with honeycomb-like nanostructure as positive electrode for high-performance hybrid supercapacitors, J. Colloid Interf. Sci., 532 (2018) 630-640.

[52] M. Chen, Y. Dai, J. Wang, Q. Wang, Y. Wang, X. Cheng, X. Yan, Smart combination of three-dimensional-flower-like MoS_2 nanospheres/interconnected carbon nanotubes for application in supercapacitor with enhanced electrochemical performance, J. Alloy. Compd., 696 (2017) 900-906.

[53] Y. Wang, Y. Lu, K. Chen, S. Cui, W. Chen, L. Mi, Synergistic effect of $Co_3O_4@C@MnO_2$ nanowire heterostructures for high-performance asymmetry supercapacitor with long cycle life, Electrochim. Acta, 283 (2018) 1087-1094.

[54] A.A. Mirghni, M.J. Madito, T.M. Masikhwa, K.O. Oyedotun, A. Bello, N. Manyala, Hydrothermal synthesis of manganese phosphate/graphene foam composite for electrochemical supercapacitor applications, J. Colloid Interf. Sci., 494 (2017) 325-337.

[55] H. Hu, B. Y. Guan, X. W. Lou, Construction of Complex CoS Hollow Structures with Enhanced Electrochemical Properties for Hybrid Supercapacitors, Chem, 1 (2016) 102-113.

[56] Z. Zhang, X. Huang, H. Wang, S.H. Teo, T. Ma, Free-standing $NiCo_2S_4@VS_2$ nanoneedle array composite electrode for high performance asymmetric supercapacitor application, J. Alloy. Compd., 771 (2019) 274-280.

[57] M. Yu, Y. Han, Y. Li, J. Li, L. Wang, Improving electrochemical activity of activated carbon derived from popcorn by $NiCo_2S_4$ nanoparticle coating, Appl. Surf. Sci., 463 (2019) 1001-1010.

[58] B. Xie, M. Yu, L. Lu, H. Feng, Y. Yang, Y. Chen, H. Cui, R. Xiao, J. Liu, Pseudocapacitive Co_9S_8/graphene electrode for high-rate hybrid supercapacitors, Carbon, 141 (2019) 134-142.

[59] H. Wang, M. Liang, D. Duan, W. Shi, Y. Song, Z. Sun, Rose-like Ni_3S_4 as battery-type electrode for hybrid supercapacitor with excellent charge storage performance, Chem. Eng. J., 350 (2018) 523-533.
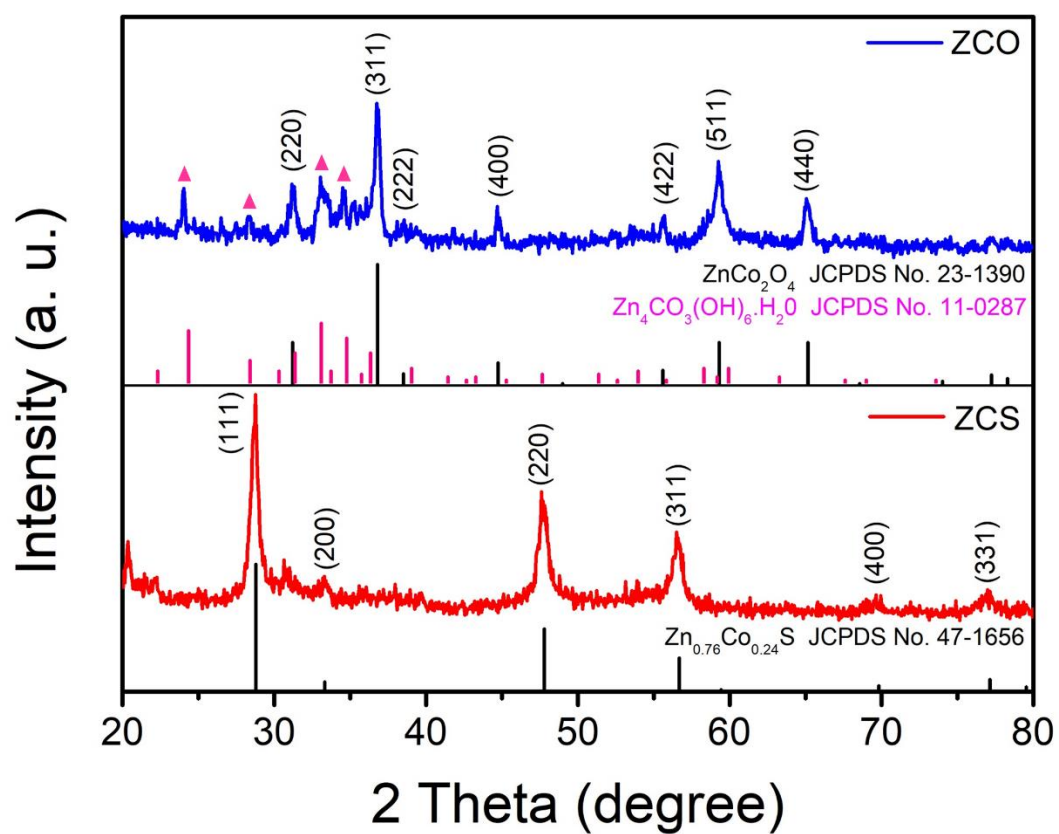
Figure Captions

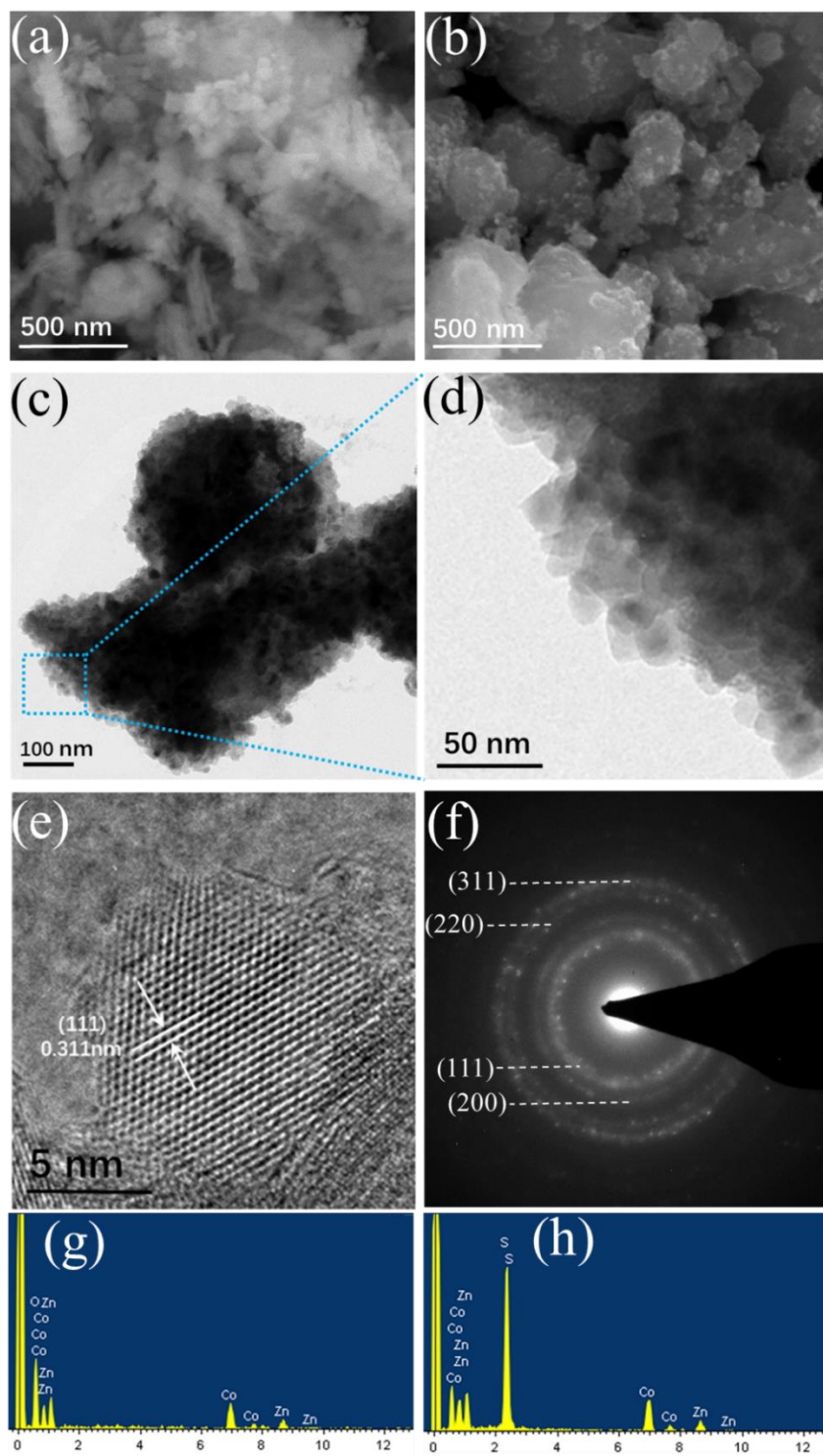Fig. 1 XRD characterization results of ZCO and ZCS NPs.

Fig. 2 SEM images of (a) ZCO and (b) ZCS NPs; (c, d) TEM images of ZCS NPs; (e) HR-TEM image of ZCS NPs; (f) SAED spectrum of ZCS NPs; EDX spectrum of (g) ZCO and (h) ZCS NPs.

Fig. 3 (a) XPS survey spectrum of the ZCO; high-resolution XPS spectra of (b) Zn 2p; (c) Co 2p and (d) O 1s.

Fig. 4 (a) XPS survey spectrum of the ZCS NPs; high-resolution XPS spectra of (b) Zn 2p; (c) Co 2p and (d) S 2p.

Fig. 5 CV curves of (a) ZCO electrode and (b) ZCS electrode at different scan rates; The linear relationships between the scan rates and the anodic/cathodic peak for (c) ZCO electrode and (d) ZCS electrode; GCD curves of (e) ZCO electrode and (f) ZCS electrode at different current densities.

Fig. 6 (a) CV curves of ZCO and ZCS electrodes at a scan rate of 10 mV s^{-1}; (b) GCD curves of ZCO and ZCS electrodes at a current density of 0.5 A g^{-1}; (c) Nyquist plots of ZCO and ZCS electrodes; (d) Specific capacitances of ZCO and ZCS electrodes at different current densities; (e) Cycling stability of the ZCS NPs electrode.

Fig. 7 (a) Schematic structure of the ASC; (b) CV curves of the AC and ZCS electrodes

at a scan rate of 10 mV s^{-1}; (c) CV curves and (d) GCD curves of ZCS NPs//AC ASC at different potential windows; (e) CV curves of ZCS NPs//AC ASC at different scan rates; (f) GCD curves of the ZCS NPs//AC ASC at different current densities.

Fig. 8 (a) Specific capacitance values of the ZCS NPs//AC ASC at different current densities; (b) Ragone plots of the ZCS NPs//AC ASC; (c) Cycling stability of the ZCS NPs//AC ASC (inset photograph is GCD curves of first and last 3 cycles); (d) lighting the LED bulb using the ZCS NPs//AC ASC.

Fig. 1 XRD characterization results of ZCO and ZCS NPs.

Fig. 2 SEM images of (a) ZCO and (b) ZCS NPs; (c, d) TEM images of ZCS NPs; (e)

HR-TEM image of ZCS NPs; (f) SAED spectrum of ZCS NPs; EDX spectrum of (g)
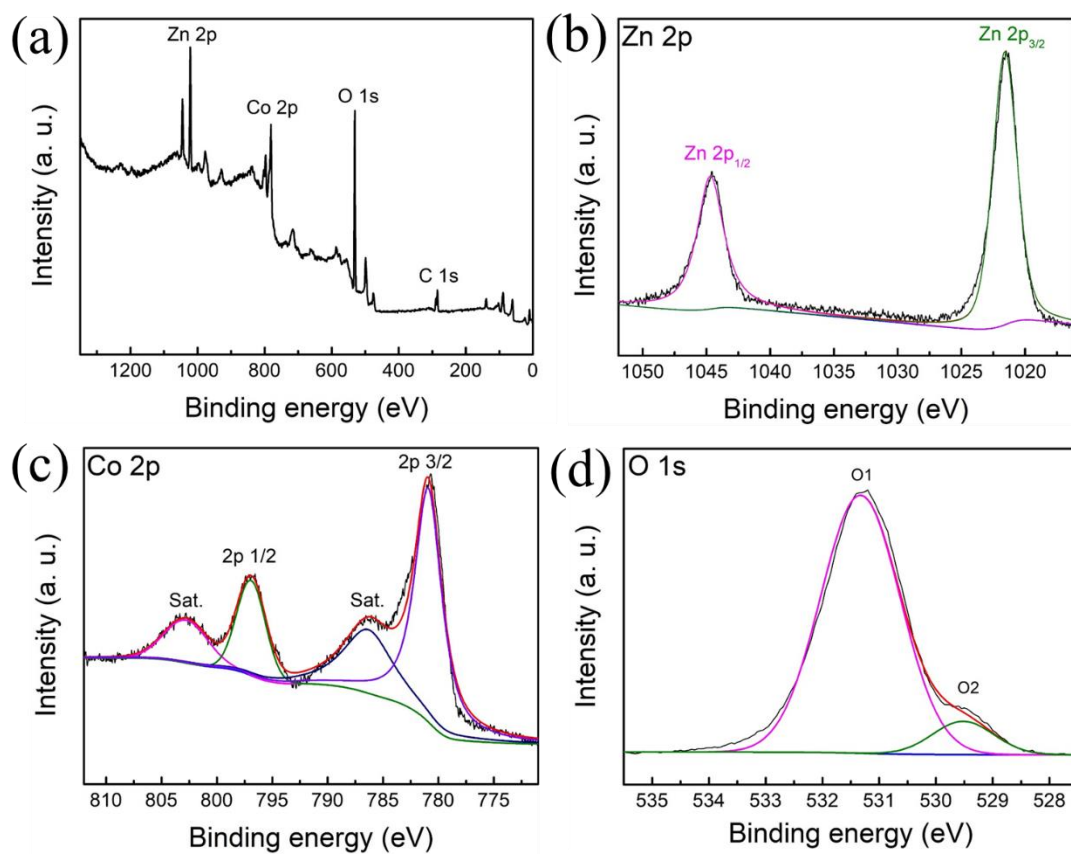
ZCO and (h) ZCS NPs.

Fig. 3 (a) XPS survey spectrum of the ZCO; high-resolution XPS spectra of (b) Zn 2p;
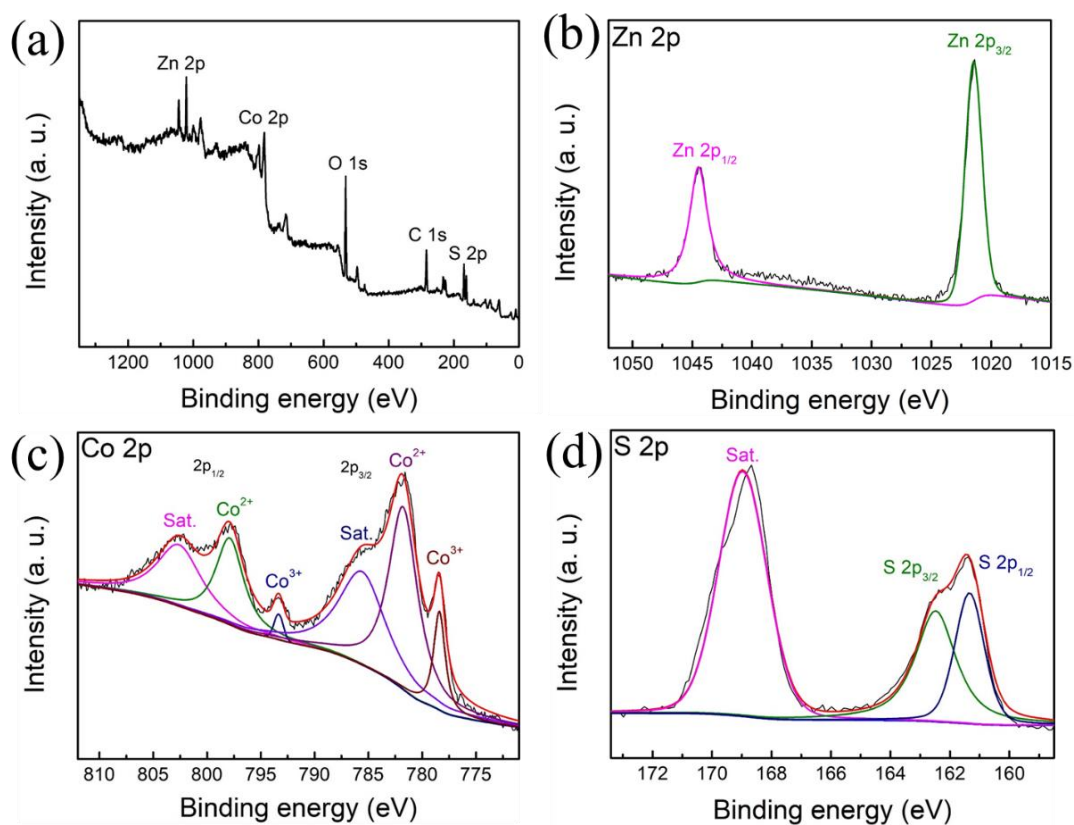
(c) Co 2p and (d) O 1s.

Fig. 4 (a) XPS survey spectrum of the ZCS NPs; high-resolution XPS spectra of (b)
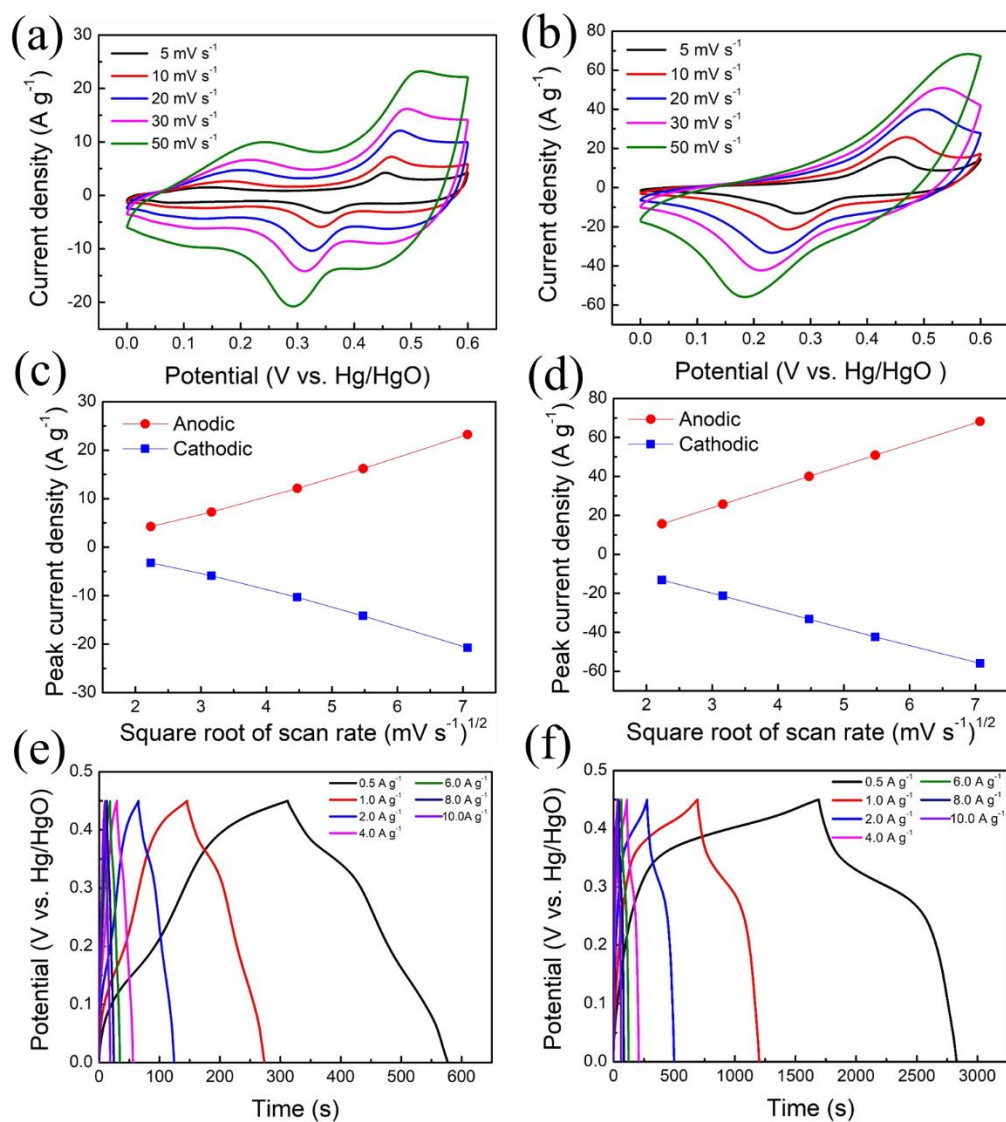
Zn 2p; (c) Co 2p and (d) S 2p.

Fig. 5 CV curves of (a) ZCO electrode and (b) ZCS electrode at different scan rates;

The linear relationships between the scan rates and the anodic/cathodic peak for (c)

ZCO electrode and (d) ZCS electrode; GCD curves of (e) ZCO electrode and (f) ZCS
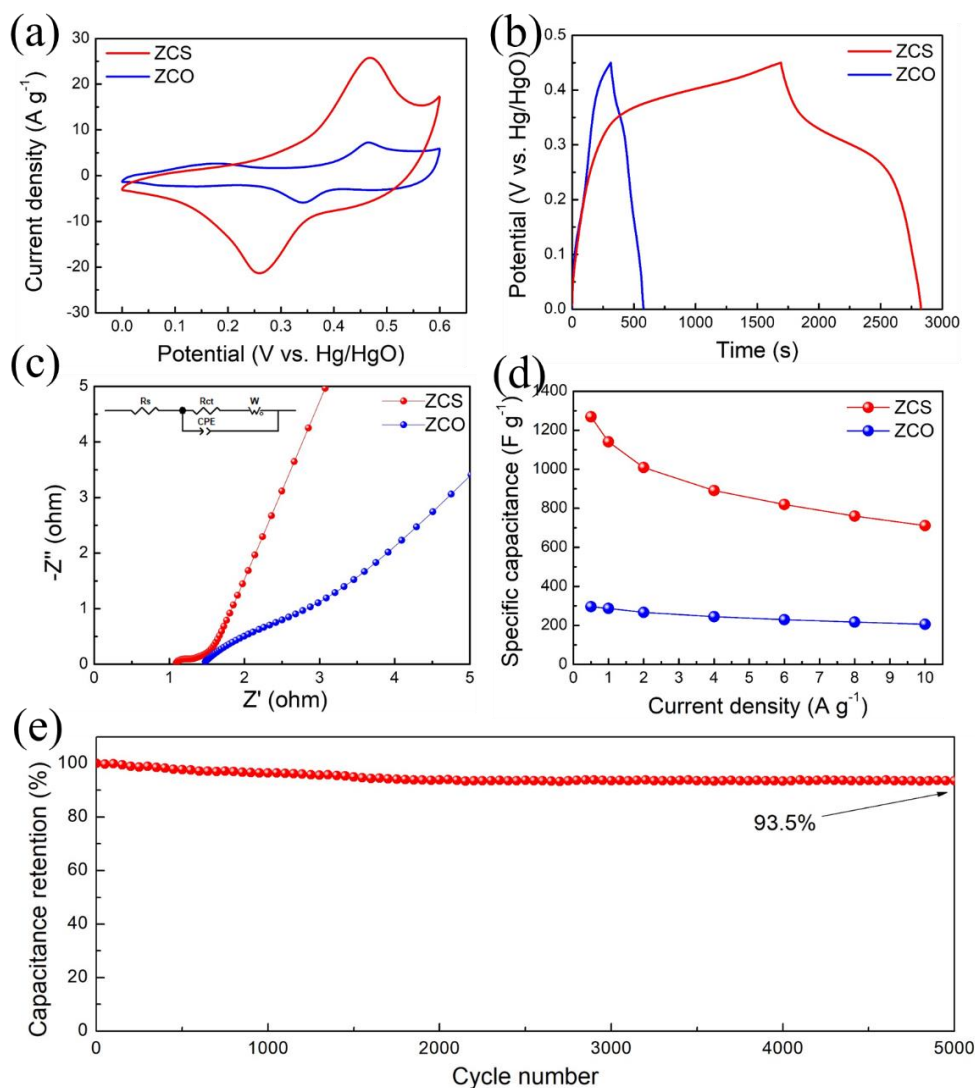
electrode at different current densities.

Fig. 6 (a) CV curves of ZCO and ZCS electrodes at a scan rate of 10 mV s^{-1}; (b) GCD curves of ZCO and ZCS electrodes at a current density of 0.5 A g^{-1}; (c) Nyquist plots of ZCO and ZCS electrodes; (d) Specific capacitances of ZCO and ZCS electrodes at different current densities; (e) Cycling stability of the ZCS NPs electrode.
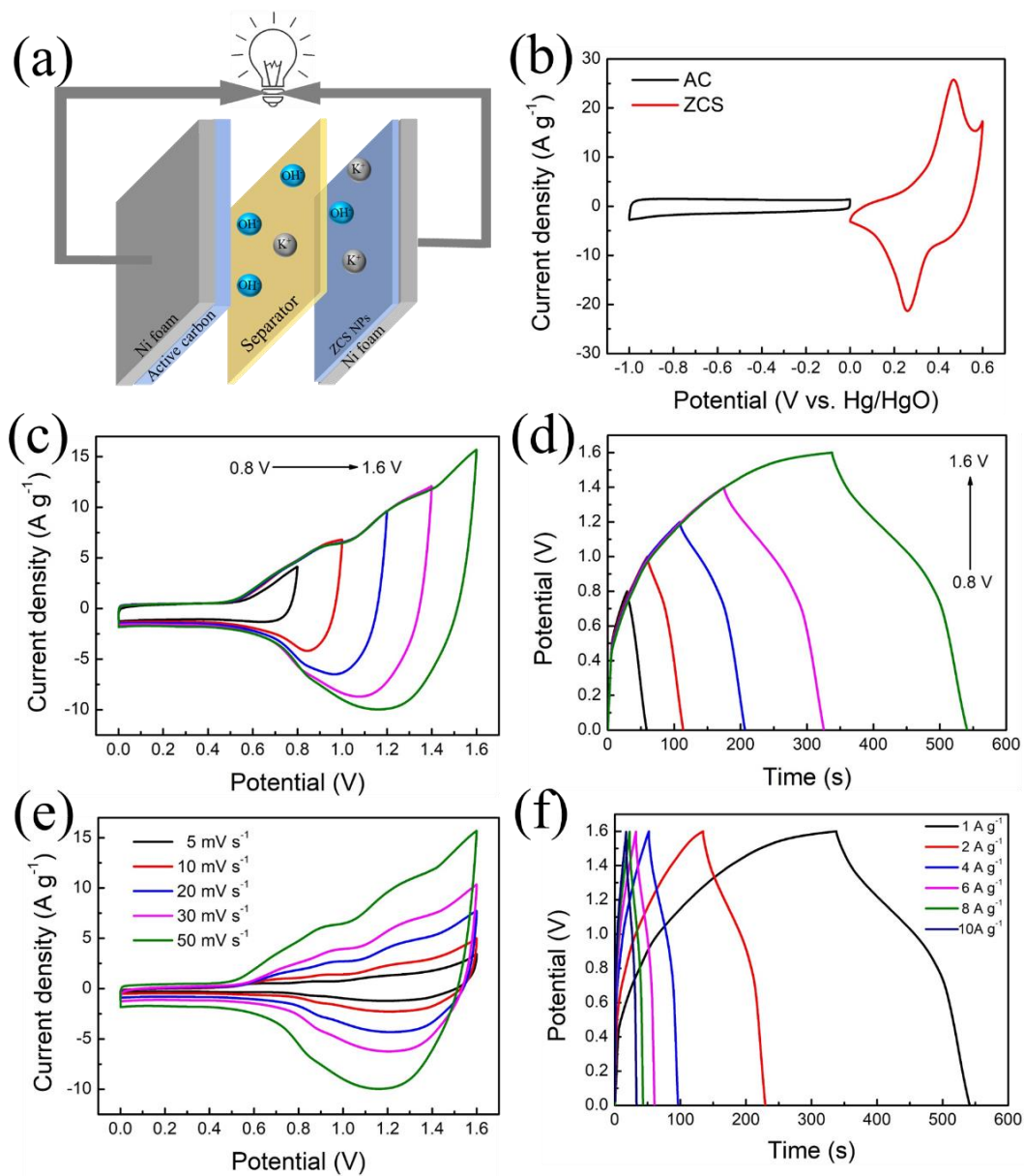
Fig. 7 (a) Schematic structure of the ASC; (b) CV curves of the AC and ZCS electrodes at a scan rate of 10 mV s^{-1}; (c) CV curves and (d) GCD curves of ZCS NPs//AC ASC at different potential windows; (e) CV curves of ZCS NPs//AC ASC at different scan rates; (f) GCD curves of the ZCS NPs//AC ASC at different current densities.
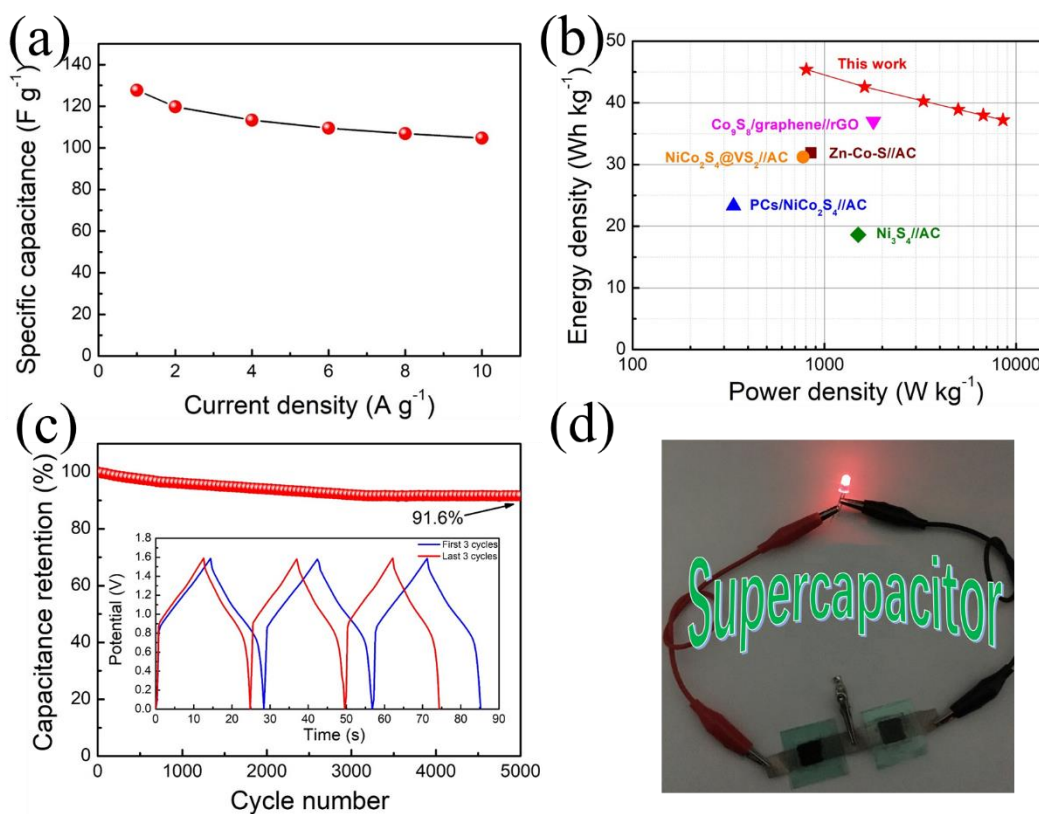
Fig. 8 (a) Specific capacitance values of the ZCS NPs//AC ASC at different current densities; (b) Ragone plots of the ZCS NPs//AC ASC; (c) Cycling stability of the ZCS NPs//AC ASC (inset photograph is GCD curves of first and last 3 cycles); (d) lighting the LED bulb using the ZCS NPs//AC ASC.